

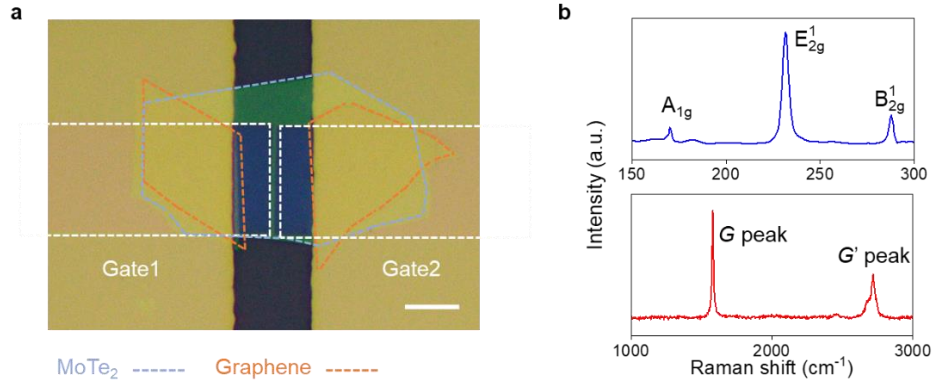
Ferroelectric-defined reconfigurable homojunctions for in-memory sensing and computing

In the format provided by the
authors and unedited

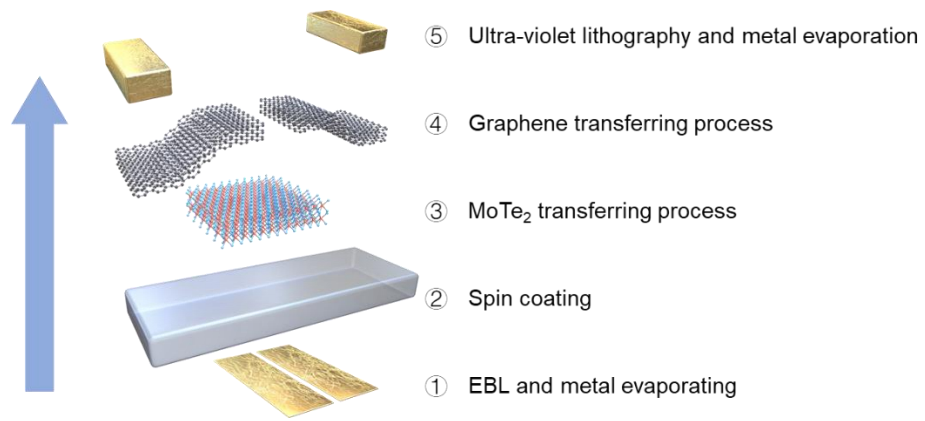
Table of contents

Supplementary Fig. 1 Characterization of the ferroelectric-defined reconfigurable 2D devices.	3
Supplementary Fig. 2 Device fabrication process following the preparation sequence from bottom to top.....	4
Supplementary Fig. 3 The evolution of junction potential profile from pn to np junction with the ferroelectric polarization.....	5
Supplementary Fig. 4 Pulse operation configuration for device transform from np to pn junction and corresponding PFM phase difference.....	6
Supplementary Fig. 5 Spatially-scanning photocurrent mapping images of the pn and np junctions, respectively	8
Supplementary Fig. 6 Pulse operation configuration for weight updating and nonlinearity fitting for LTP/LTD process.....	9
Supplementary Fig. 7 Retention property of the positive and negative weight defined ferroelectric domains and long-term stability of all the 51 photoresponsivity states.	10
Supplementary Fig. 8 Endurance property of P(VDF-TrFE) in the capacitor structure.....	11
Supplementary Fig. 9 Response speed of the device in the np and pn configurations.....	12
Supplementary Fig. 10 The programming voltage amplitude could be reduced by decreasing the ferroelectric thickness.....	13
Supplementary Fig. 11 Electrical characteristics of the device in the array with transferred Au electrodes	15
Supplementary Fig. 12 Raman spectra of the 27 MoTe ₂ in the sensor array.....	16
Supplementary Fig. 13 Weight distribution histograms of all 27 photodiodes in the sensor array.....	17
Supplementary Fig. 14 Photocurrent accumulation verification in the sensor array.....	18
Supplementary Fig. 15 Different Sobels for image edge detection.....	19
Supplementary Fig. 16 Feature map of the combined right and top edge detection results.....	20
Supplementary Fig. 17 The convolutional neural network (CNN) for image recognition, configured with the reconfigurable sensor array as convolutional layer.	21
Supplementary Fig. 18 The detailed communication process between the IMSC and the robot dog.....	23
Supplementary Fig. 19 Macroscopic image of the IMSC chip, where ‘L’, ‘T’ and ‘J’ patterns were projected onto the sensor array through hard masks.....	24
Supplementary Fig. 20 Training process and final weights distribution of our sensor array.....	25
Supplementary Fig. 21 Hardware implementation of image classification when introducing noise	

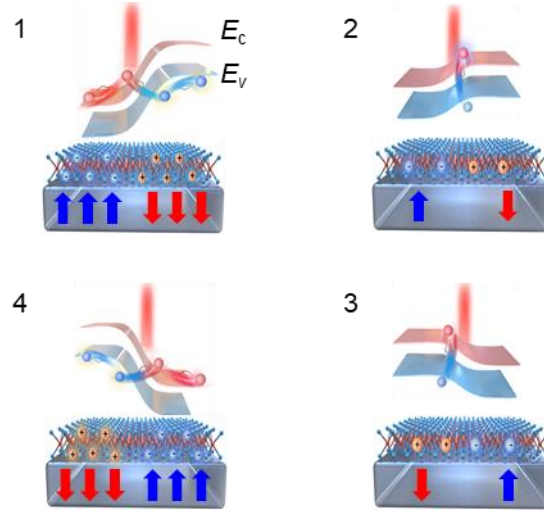
into the patterns.....	26
Supplementary Fig. 22 the comparison between our devices and different neuromorphic vision sensors.....	27
Supplementary Fig. 23 The operating frequency difference of the IMSC computing compared with the conventional sensory computing architecture.....	28
References.....	30



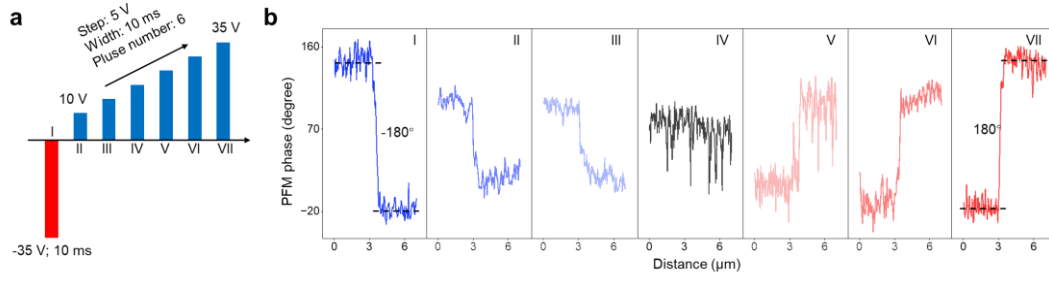
Supplementary Fig. 1 | Characterization of the ferroelectric-defined reconfigurable 2D devices. **a**, An optical microscope image of the ferroelectric-defined reconfigurable 2D homojunctions with the material boundaries artificially colored. The scale is 10 μm . **b**, Raman spectra of MoTe₂ and Graphene, indicating high-quality crystal structure.



Supplementary Fig. 2 | Device fabrication process following the preparation sequence from bottom to top.

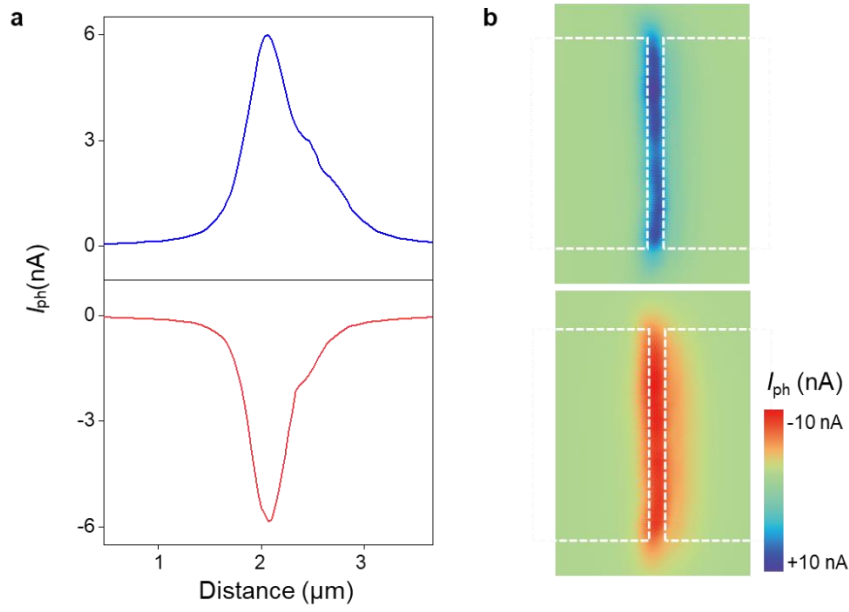


Supplementary Fig. 3 | The evolution of junction potential profile from pn to np junction with the ferroelectric polarization. The ferroelectric domains can be gradually switched oppositely by applying voltage pulse on the split gates, resulting in a reduction of the pn junction built-in electric field, hence the photoresponsivity. When the ferroelectric-defined built-in electric field comes to zero, the photoresponsivity equals to 0. By continuing to apply voltage pulse, the ferroelectric domains are reversed, so as the junction potential profile, giving rise to a negative photoresponsivity. The negative photoresponsivity comes to its maximum when the left/right part of the ferroelectric is fully polarized down/up.

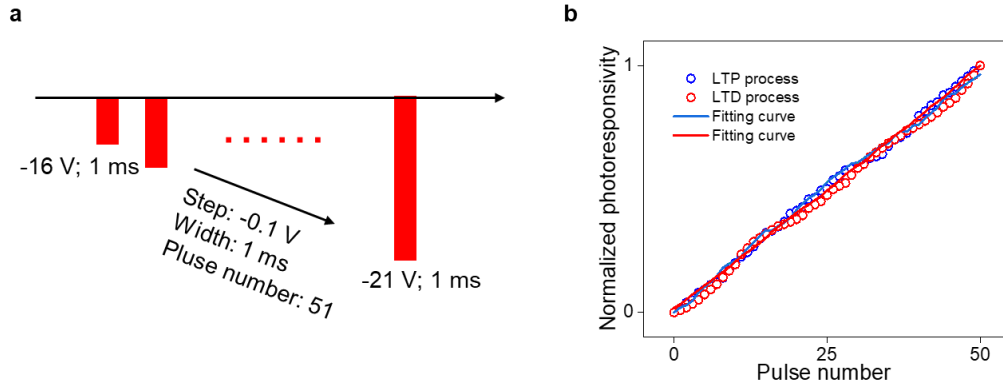


Supplementary Fig. 4 | Pulse operation configuration for device transform from np to pn junction and corresponding PFM phase difference. **a**, Pulse operation configuration for linear photoresponsivity tunability. In state I, the left/right ferroelectric domain is downward/upward with a phase difference of -180° as demonstrated by the PFM phase image, affirming the fully polarized ferroelectric domains. The corresponding output curve demonstrates obvious rectification characteristics. After applying a reverse voltage pulse to the split gates, a portion of the domains are switched and the phase difference is thus reduced (state II). The resulting output curve shows a smaller current at negative V_{sd} and a higher current at positive V_{sd} , meaning a weaker rectification behavior compared with state I. As more domains are switched, the ferroelectric-induced built-in electric field reduces, resulting in a less obvious rectification output curve (state III). When the domains are manipulated to a mixed configuration (state IV), the rectification behavior disappears, and a symmetric output curve is observed. By continuing to apply pulse voltage, the ferroelectric domains are reversed, and the current at positive V_{sd} is larger than that at negative V_{sd} , demonstrating gradually

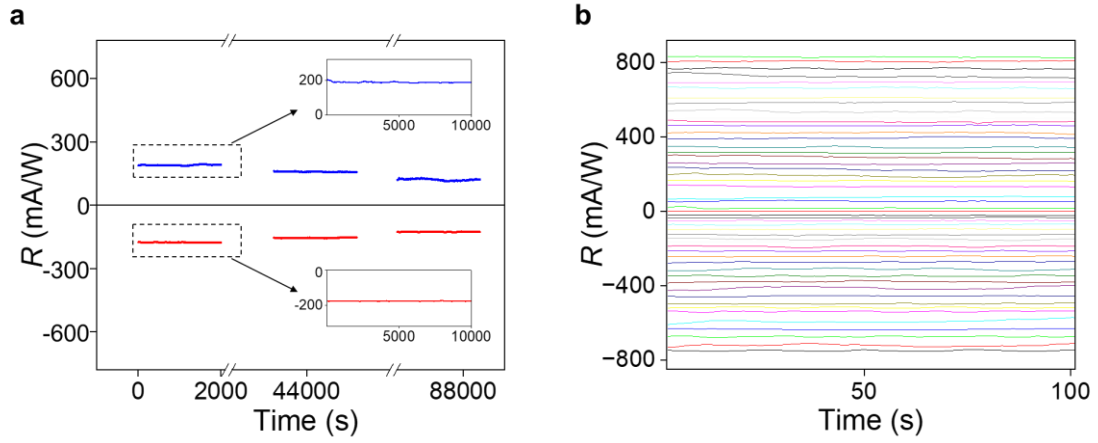
enhanced forward rectification characteristics (states V-VII). Eventually, a totally polarized pn junction with almost the same turn-on and turn-off current as the np junction in State I is obtained. **b**, PFM phase difference of the 7 states in Fig. 2e from -180° to 180° .



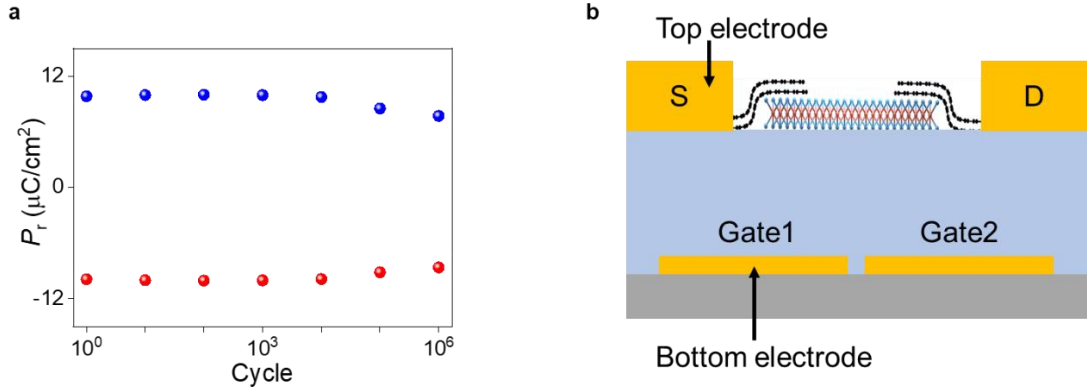
Supplementary Fig. 5 | Spatially-scanning photocurrent mapping images of the pn and np junctions, respectively. **a**, Location distribution of photocurrent of the np (upper panel) and pn (lower panel) junctions along the channel. **b**, spatially-scanning photocurrent mapping images of the np (upper panel) and pn (lower panel) junctions, whose photocurrent occurs exactly between the split gates.



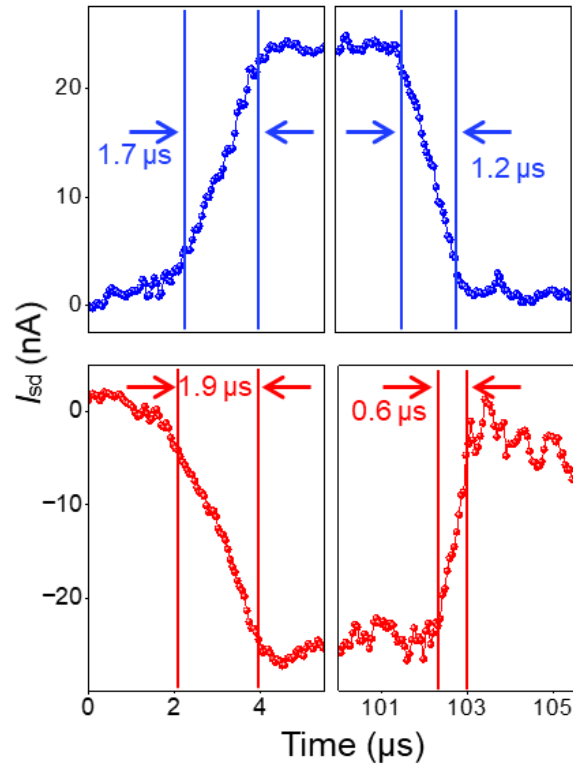
Supplementary Fig. 6 | Pulse operation configuration for weight updating and nonlinearity fitting for LTP/LTD process. **a**, A series of pulse voltage with amplitude changes from -16 V to -21 V in increments of -0.1 V and pulse width of 1 ms is applied in Fig. 3c for LTP process. **b**, LTP/LTD process and corresponding nonlinearity fitting results. A nonlinearity value for LTP/LTD process is fitted to be 0.12/-0.12, respectively.



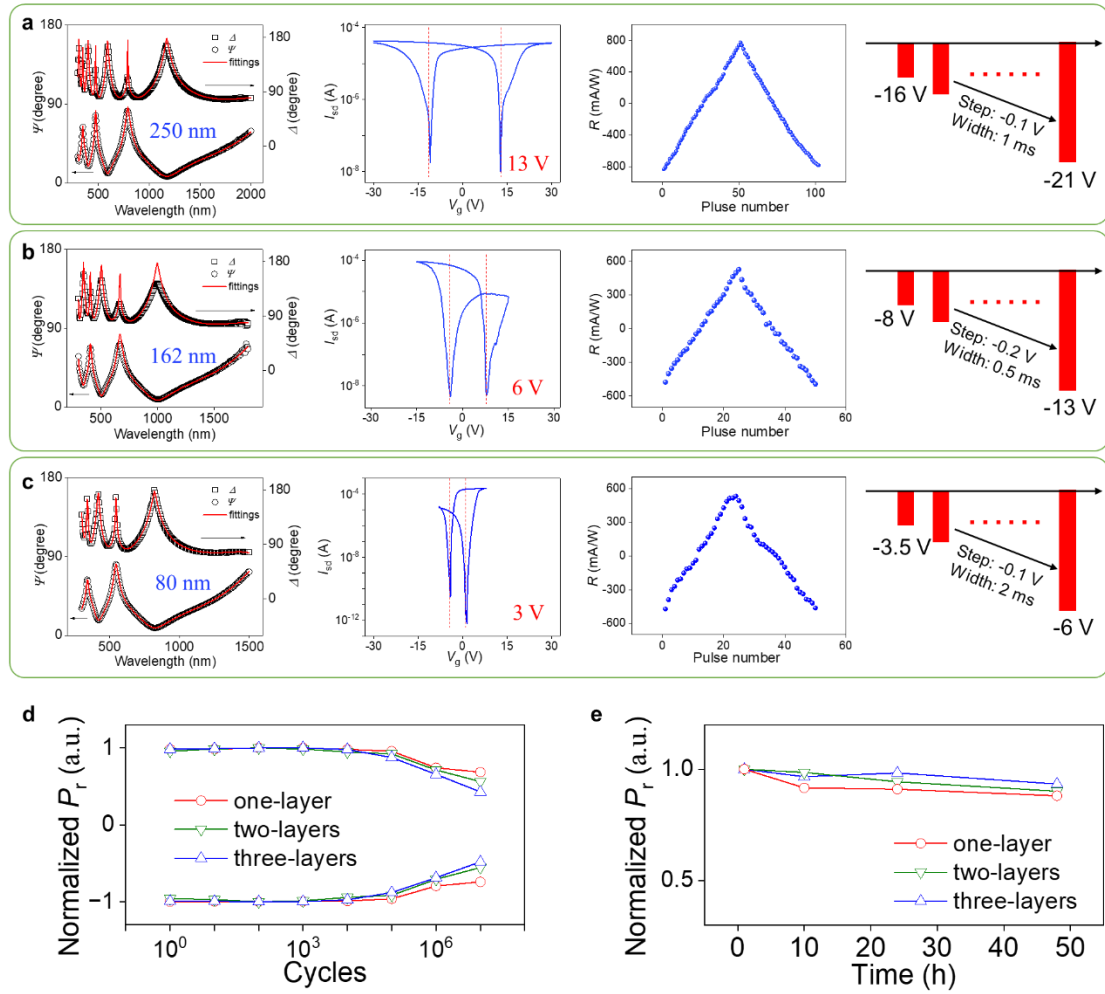
Supplementary Fig. 7 | Retention property of the positive and negative weight defined ferroelectric domains and long-term stability of all the 51 photoresponsivity states. **a**, Both the positive and negative photoresponsivity remains nearly unchanged over 24 h. The enlarge photoresponsivity is very stable over 10000 s. **b**, The long-term stability of all the 51 photoresponsivity states (25 positive states, 25 negative states and 1 "zero" state), showing distinguishable weight states.



Supplementary Fig. 8 | Endurance property of P(VDF-TrFE) in the capacitor structure. **a**, Both positive and negative remnant polarization of P(VDF-TrFE) shows negligible deterioration after 10^6 cycles. **b**, Schematic of the 2D device served as P(VDF-TrFE) capacitor structure. The top electrode is the source terminal, and the bottom electrode is Gate1.

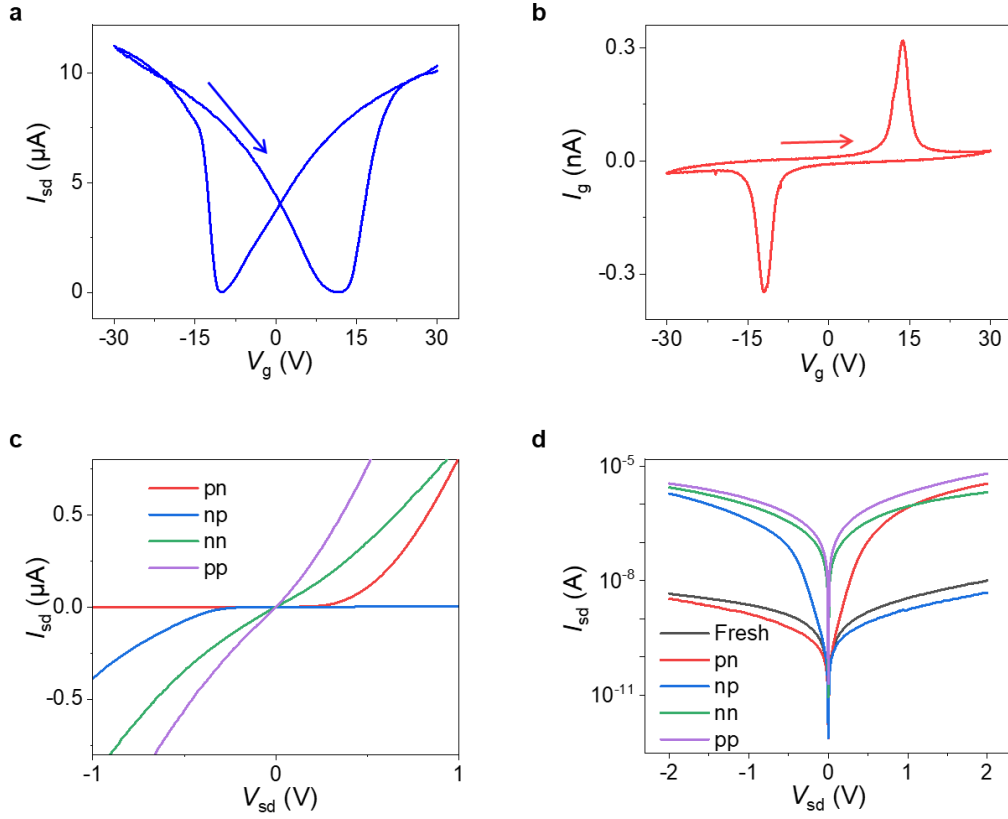


Supplementary Fig. 9 | Response speed of the device in the np and pn configurations. The rise and fall edges for positive (upper panel) and negative (lower panel) photoresponsivity, exhibiting a fast photoresponse with rising time of $1.9 \mu s$ and decaying time of $0.6 \mu s$ (negative photoresponse).

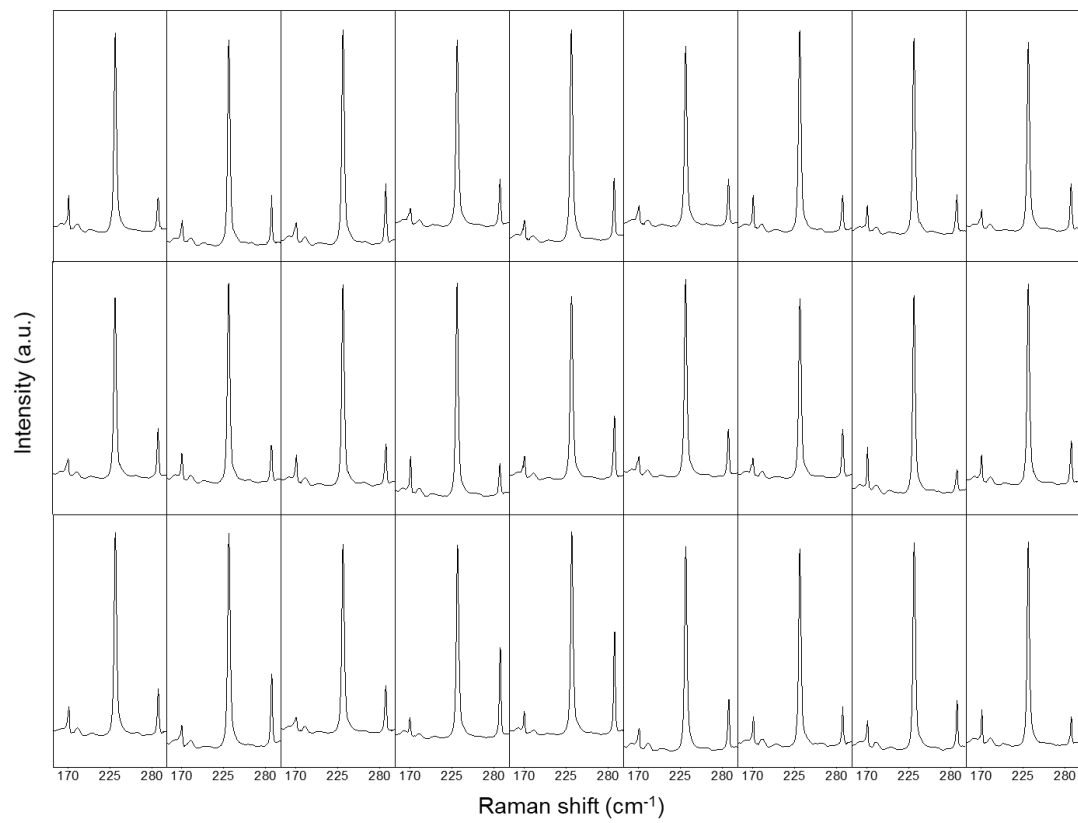


Supplementary Fig. 10 | The programming voltage amplitude could be reduced by decreasing the ferroelectric thickness. The The transfer characteristics and LTP/LTD programming scheme for device with three-layers (a), two-layers (b), and one-layer (c) P(VDF-TrFE). P(VDF-TrFE) thickness was obtained by ellipsometry. Experimental and the corresponding fitted ellipsometry spectra (Ψ and Δ) of P(VDF-TrFE) films at the incidence angle of $\Theta = 70^\circ$ are demonstrated. The red lines show the Gaussian model fittings which give the thickness values of 250 ± 2 nm, 162 ± 1 nm and 80 ± 1 nm, respectively. The endurance (d) and retention (e) properties of the devices are investigated using the P(VDF-TrFE) capacitor

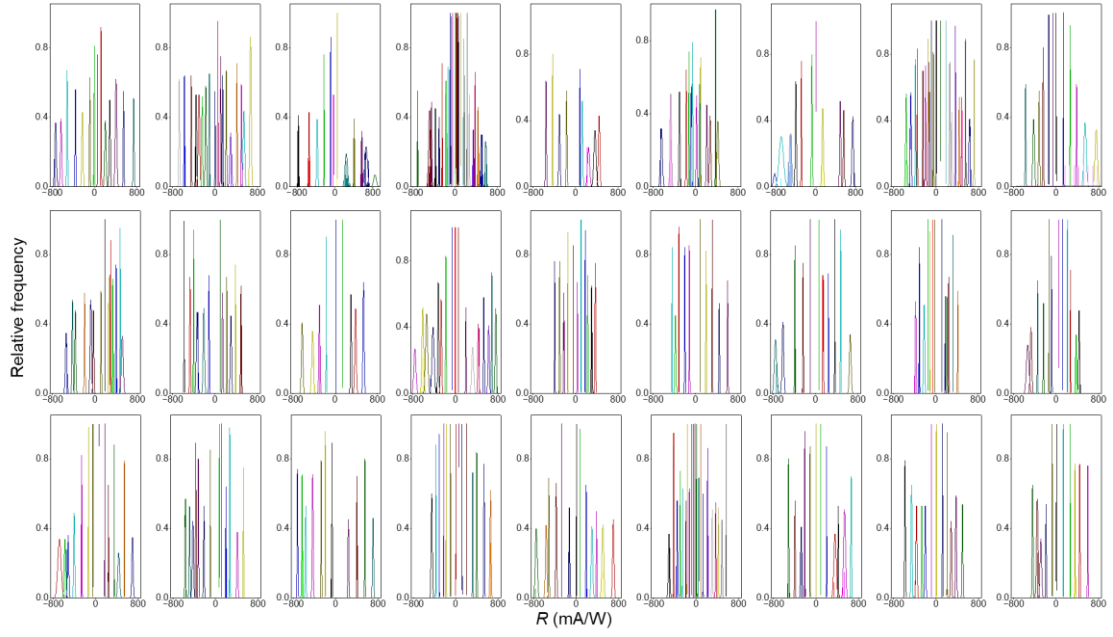
structure. A polarization loss of 25%, 40%, and 50% is demonstrated after 10^7 cycles for one-layer, two-layers, and three layers P(VDF-TrFE), respectively. A polarization loss of 12%, 10%, and 7% is shown after 48 h for one-layer, two-layers, and three layers P(VDF-TrFE), respectively. P_r represents the the remanent polarization. Devices with thinner ferroelectric layer, characterized as better endurance property, are suitable for tasks involving frequent training. On the other hand, inference tasks rely on pre-stored weights, and the retention property is critical. Devices with thicker ferroelectric layer are more suitable for this scenario.



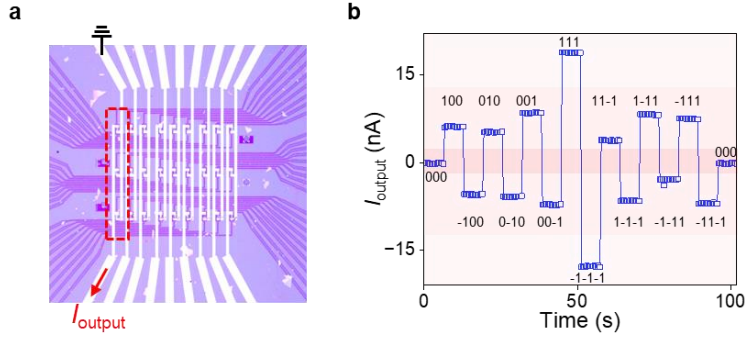
Supplementary Fig. 11 | Electrical characteristics of the device in the array with transferred Au electrodes. a, I_{sd} – V_g characteristics at room temperature of a representative MoTe₂ device in the array. Symmetric I_{sd} – V_g curve indicates excellent bipolar nature. **b,** I_g – V_g characteristics of the device. Two apparent typical ferroelectric switching peaks are observed near ± 14 V. **c,d,** I_{sd} – V_{sd} characteristic curves for pn, np, nn, pp and fresh homojunctions plotted on linear (c) and logarithmic scale (d).



Supplementary Fig. 12 | Raman spectra of the 27 MoTe₂ in the sensor array. The raman spectra shows good uniformity of the 2D materials.



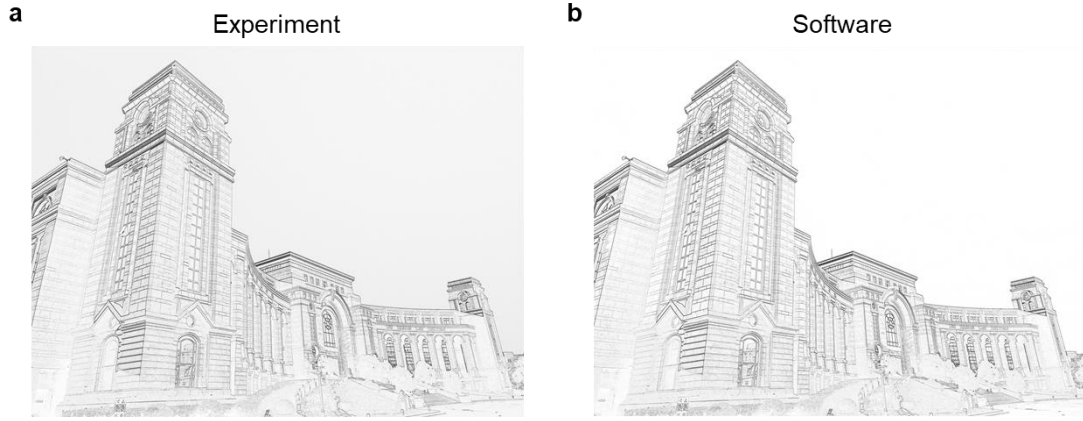
Supplementary Fig. 13 | Weight distribution histograms of all 27 photodiodes in the sensor array. All the devices in the array shows good ferroelectric weight tunability.



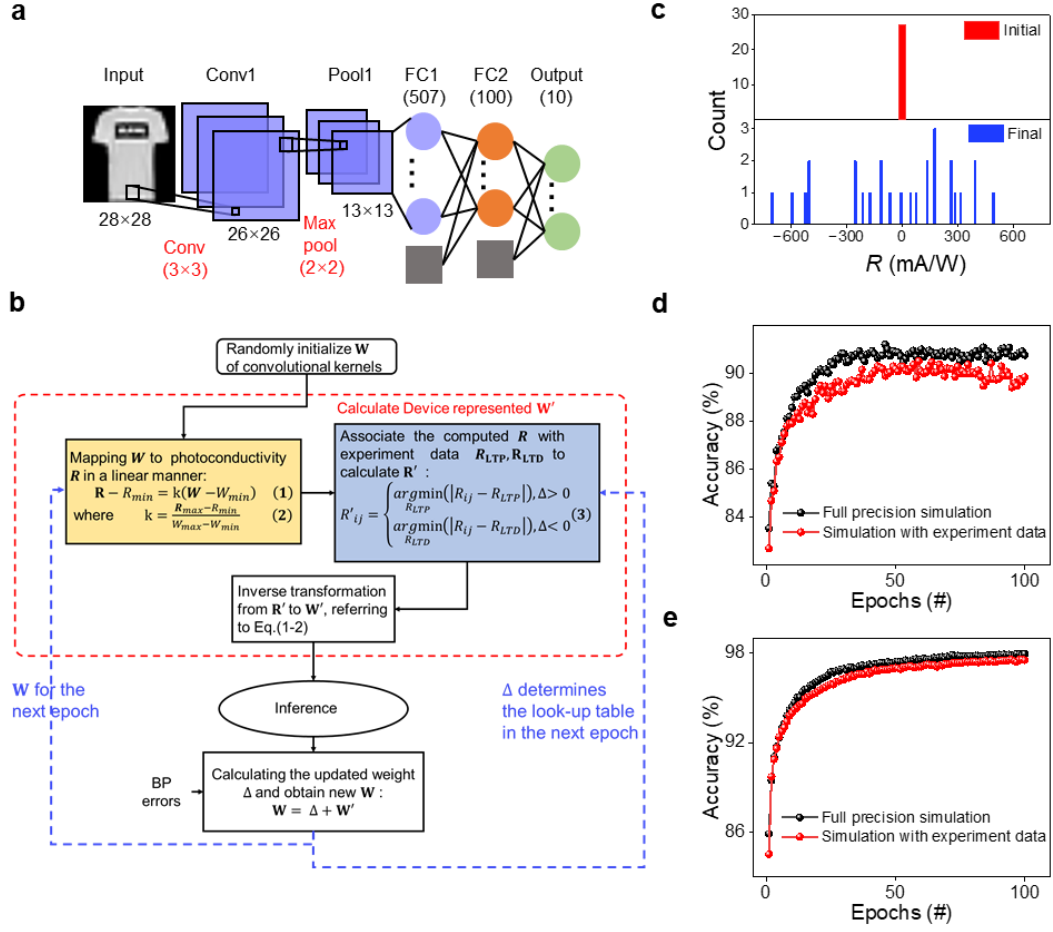
Supplementary Fig. 14 | Photocurrent accumulation verification in the sensor array. **a**, the devices in the first column are selected to verify the accumulation of photocurrent from every individual sensor. **b**, The output photocurrent of Column 1 for different 15 different photoresponsivity configurations. Here, state 1,-1 and 0 represents the largest positive, negative and zero photoresponsivity. Therefore, (100) represents $R_{11}=1$, $R_{41}=0$ and $R_{71}=0$. This description also applies to other photoresponsivity configurations. The output current of this column is exactly the sum of the photocurrents of the three devices, confirming the photocurrent accumulation results.

$$\begin{array}{ccc}
 \mathbf{a} \begin{bmatrix} -1 & 0 & +1 \\ -2 & 0 & +2 \\ -1 & 0 & +1 \end{bmatrix} & \mathbf{b} \begin{bmatrix} +1 & +2 & +1 \\ 0 & 0 & 0 \\ -1 & -2 & -1 \end{bmatrix} & \mathbf{c} \begin{bmatrix} 0 & -1 & 0 \\ -1 & 5 & -1 \\ 0 & -1 & 0 \end{bmatrix} \\
 \text{Right Sobel} & \text{Top Sobel} & \text{Sharpen}
 \end{array}$$

Supplementary Fig. 15 | Different Sobels for image edge detection. a-c, Sobels with right edge detection (a), top edge detection (b) and sharpen functions (c).

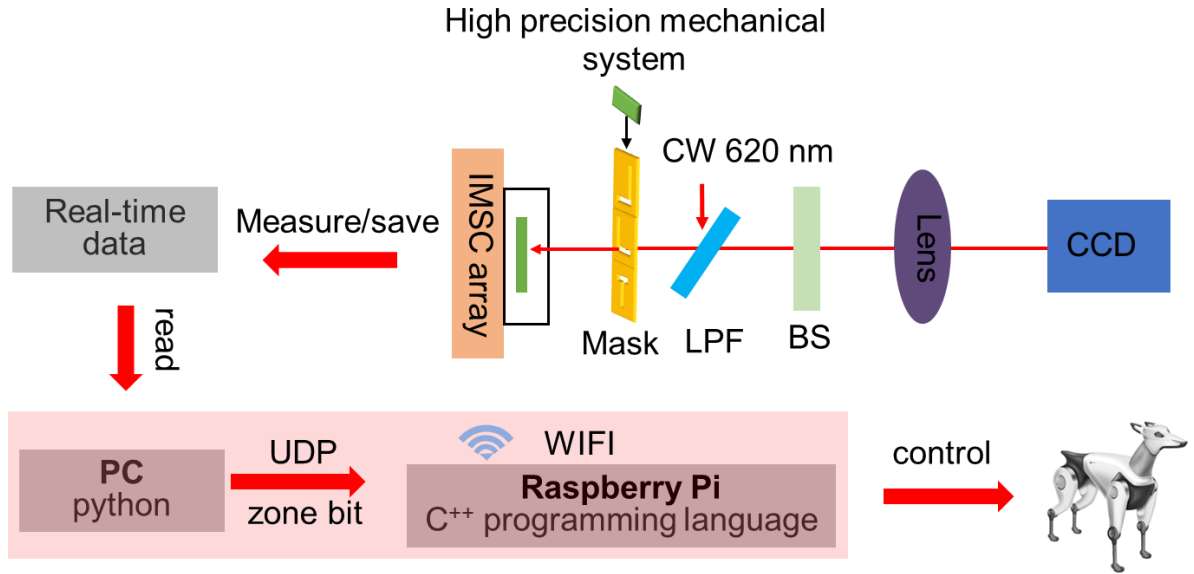


Supplementary Fig. 16 | Feature map of the combined right and top edge detection results. a,b, Right edge detection result R_L and top edge detection result R_T are combined by $\sqrt{R_L^2 + R_T^2}$ to obtain the feature map of edges¹, where experiment (a) and software results (b) match well.

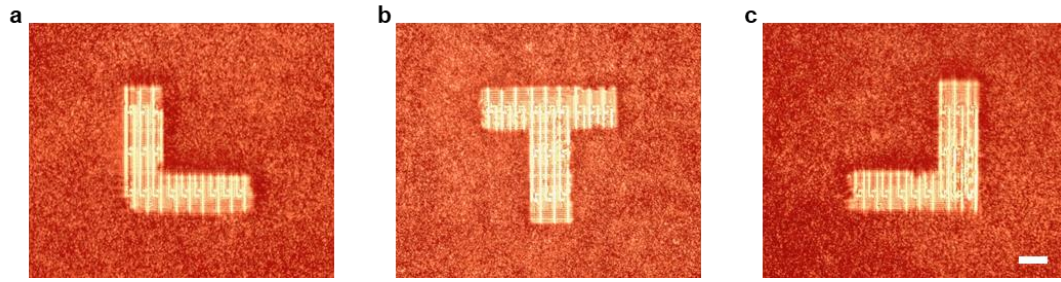


Supplementary Fig. 17 | The convolutional neural network (CNN) for image recognition, configured with the reconfigurable sensor array as convolutional layer. a, Illustration of the convolutional neural network for image recognition, which consists of 1 input layer, 1 convolutional layer (configured with our sensor array), 1 pool layer, 2 fully connected layers and 1 output layer. **b**, The training processes of the CNN with experimental LTP-LTD curve. The CNN is trained off-line according to the experimental LTP-LTD curve in Figure 3c. Here, the Fashion Modified National Institute of Standard and Technology (MNIST) dataset is used for training using backpropagation approach **c**, The initial (red) and final (blue) weight distribution of sensor array. **d**, Comparisons of the image recognition

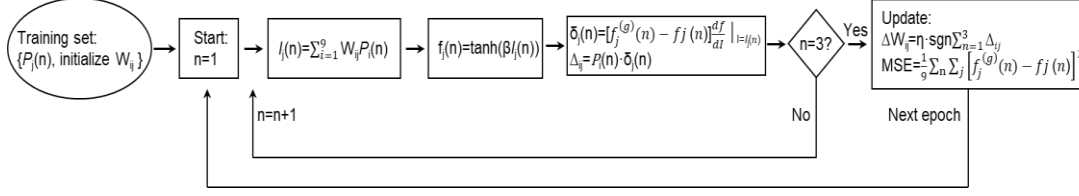
accuracy between the simulation with experiment data and full precision simulation results. The accuracy reaches $\sim 90\%$ after 50 epochs, which is consistent with the full precision simulation results ($\sim 91\%$). **e**, Image recognition accuracy for handwritten MNIST database. We performed simulations based on handwritten MNIST datasets, with the accuracy reaching up to 98%.



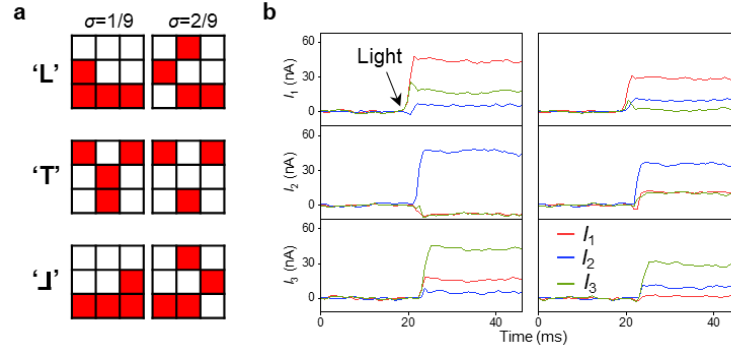
Supplementary Fig. 18 | The detailed communication process between the IMSC and the robot dog. When the specified optical signal is irradiated on the device, the photocurrent of the three-way channel is collected through labview and saved in real time under the specified path of the working computer. Then, the saved data on our computer was read through a python program. The data of the three channels will be processed and judged by the designated program. At the meantime, the computer emits a wifi hotspot, and the raspberry Pi on the robot dog links to the hotspot. The result of python's judgment is sent to Raspberry Pi over user datagram protocol (UDP) in the form of flag bits. By running C++ program, Raspberry Pi converts the obtained flag bits into control signals and sends them to the robot dog, so as to realize the goal of intelligent control of the robot dog movement by sensing light patterns on the chip.



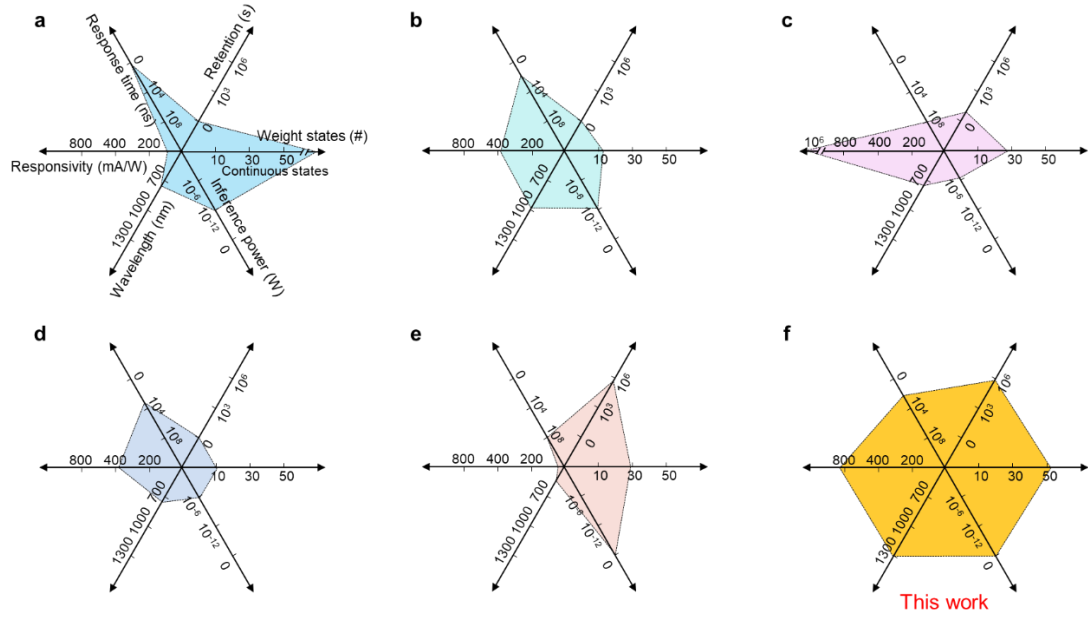
Supplementary Fig. 19 | Macroscopic image of the IMSC chip, where ‘L’ (a), ‘T’ (b) and ‘J’ (c) patterns were projected onto the sensor array through hard masks. The scale is 100 μm .



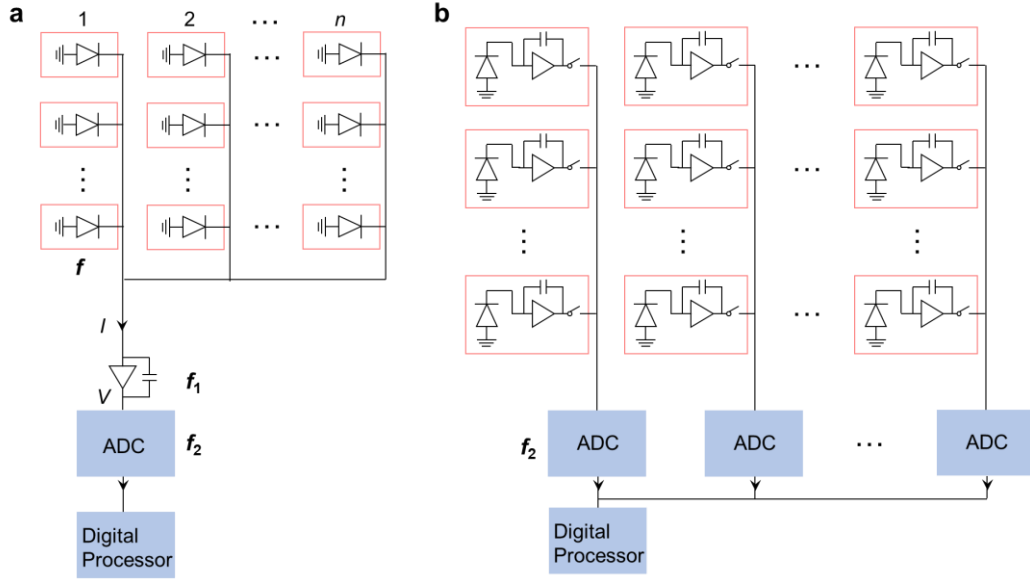
Supplementary Fig. 20 |. Training process of the sensor array. The responsivities were updated by backpropagation². Here, $P_j(n)$ is the input light power for the n th input pattern, W_{ij} is tunable weights, f_j is the perceptron's j th outputs, $f_j^{(g)}(n)$ is the target value of the j th output for the n th input pattern, Δ_{ij} is delta-rule weight increments calculating with $\delta_j(n)$, β is a parameter controlling the function's nonlinearity, η is a constant that scales the training rate.



Supplementary Fig. 21 | Hardware implementation of image classification when introducing noise into the patterns. a, Illustrations of the 3×3 patterns with noise. **b**, Output currents for different patterns with noise, where current for target pattern is still well separated with those for other patterns.



Supplementary Fig. 22 | the comparison between our devices and different neuromorphic vision sensors. a-e, The figures of merit of different neuromorphic vision sensors extracted from Ref. 3-7³⁻⁷, respectively. **f,** The figures of merit of our ferroelectric-defined reconfigurable 2D sensors.



Supplementary Fig. 23 | The operating frequency difference of the IMSC computing compared with the conventional sensory computing architecture.

a, Schematic of our IMSC computing flow. **b**, Schematic of the conventional sensory computing architecture. Assuming that the sensor array is $n \times n_2$ and a typical analog front-end (AFE) and analog digital converter (ADC) operating frequency of f_1 and f_2 MHz, our IMSC operating frequency is mainly limited by the response speed of our sensors ($f \sim 1$ MHz in Supplementary Fig. 9), f_1 and f_2 . Therefore, the operating frequency is

calculated to be $\frac{1}{\frac{1}{f} + \frac{1}{f_1} + \frac{1}{f_2}}$ MHz. For the conventional architecture, the

speed of the photodetectors is very fast (in the ns range), which can be neglected, so the operating frequency is primarily influenced by the serial operation of the column-parallel ADC module. Therefore, the operating frequency is calculated to be $\frac{1}{\frac{1}{f_1} + n \times \frac{1}{f_2}}$ MHz. Taking the typical value of

$f_1=1$, $f_2=0.2$, and $n=3$ into account⁸, the operating frequency of our IMSC

and the conventional computing architecture are calculated to be ~ 0.14 MHz and 0.06 MHz, respectively. This operating frequency difference will be enlarged as the sensor array scales up (n is increased) and the response speed of our sensor is improved (f is increased). For example, the operating frequency difference can exceed 500 times for a commonly used 640×512 sensor array.

References

1. Lin, P. *et al.* Three-dimensional memristor circuits as complex neural networks. *Nat. Electron.* **3**, 225-232 (2020).
2. Rumelhart, D.E., Hinton, G.E. & Williams, R.J. Learning representations by back-propagating errors. *Nature* **323**, 533-536 (1986).
3. Mennel, L. *et al.* Ultrafast machine vision with 2D material neural network image sensors. *Nature* **579**, 62-66 (2020).
4. Pi, L. *et al.* Broadband convolutional processing using band-alignment-tunable heterostructures. *Nat. Electron.* **5**, 248-254 (2022).
5. Zhang, Z. *et al.* All-in-one two-dimensional retinomorphic hardware device for motion detection and recognition. *Nat. Nanotechnol.* **17**, 27-32 (2022).
6. Wang, C.Y. *et al.* Gate-tunable van der Waals heterostructure for reconfigurable neural network vision sensor. *Sci. Adv.* **6**, eaba6173 (2020).
7. Cui, B. *et al.* Ferroelectric photosensor network: an advanced hardware solution to real-time machine vision. *Nat. Commun.* **13**, 1707 (2022).
8. Kim, H.-J. 11-bit Column-Parallel Single-Slope ADC With First-Step Half-Reference Ramping Scheme for High-Speed CMOS Image Sensors. *IEEE Journal of Solid-State Circuits* **56**, 2132-2141 (2021).